

scientific data



OPEN

DATA DESCRIPTOR

Svalbard Marginal Ice Zone 2024: A distributed network of temperature, waves, and sea ice drift observations

Malte Müller^{1,2}✉, Jean Rabault³, Chiara de Geeter^{1,2}, Cyril Palerme¹, Bikas Chandra Bhattacharai⁴, Fabrice Collard⁵, Steinar Eastwood⁶, Sylvain Herlédan⁵, Gáute Hope⁶, Nick Hughes⁶, Marius O. Jonassen⁷, Jørn Kristiansen¹, Frank Nilsen⁷ & Olaf Weisser⁴

The coupling of weather, sea-ice, ocean, and wave forecasting systems has been a research priority for improving Arctic prediction capabilities. However, the complexity of the underlying physical processes and the difficulty of obtaining observations on representative spatial and temporal scales present significant challenges, particularly in the Marginal Ice Zone (MIZ). The primary objective of the Svalbard Marginal Ice Zone Campaign 2024 (SvalMIZ-24) was to establish a network of observations with a spatial distribution that enables a representative comparison between *in situ* measurements and gridded model data. The key variables that were measured are air and surface temperatures, sea-ice drift, and wave energy spectra. Within the main observation period, a persistent cold air outbreak as well as a warm air intrusion event, coinciding with the formation of an intense wave system propagating into the MIZ was captured. This dataset provides valuable insights into atmosphere-ice-ocean interactions in the MIZ and serves as a resource for future studies, model validation, and intercomparison efforts aimed at improving Arctic forecasting systems.

Background & Summary

The Arctic region is undergoing rapid climatic changes, making it crucial to enhance our understanding of atmosphere-ice-ocean interactions¹. The Marginal Ice Zone (MIZ) is a dynamic and complex area where the coupled sea-ice, ocean, wave, and atmospheric processes are challenging to observe, understand, and simulate. As Arctic temperatures rise and sea-ice volume diminishes², the shape, location and size of the MIZ is changing^{3,4}, particularly in summer, leading to a changed exposure of open water to atmospheric forcing and wave action⁵. Ultimately, this development will also open up new shipping routes alongside navigational hazards that put strong demands on the accuracy of coupled Arctic forecasting systems⁶.

Observations within the MIZ are rare, primarily due to the region's highly dynamic nature, which significantly limits the operational lifespan of deployed instruments and provides challenging environmental conditions and logistical difficulties for observational campaigns. There have been several initiatives with a focus on monitoring sea ice drift and wave energy propagation in the MIZ using drifting buoys deployed on the sea-ice^{7–11}. By contrast, atmospheric *in situ* measurements in the MIZ are still rare and predominantly collected through research expeditions utilizing vessels and aircraft^{12–14}, or campaigns in close vicinity to the sea ice edge that study, for example, cold air outbreaks^{15,16}.

Generally, a key challenge in utilizing *in situ* observations for model comparison lies in their spatial and temporal representativeness, hence distributed networks of observations are important for the evaluation of model

¹Norwegian Meteorological Institute, Development Centre for Weather Forecasting, Oslo, 0313, Norway. ²University of Oslo, Department of Geosciences, Oslo, 0313, Norway. ³Norwegian Meteorological Institute, IT Department, Oslo, 0313, Norway. ⁴Norwegian Meteorological Institute, Observation Department, Oslo, 0313, Norway. ⁵OceanDataLab, Locmaria-Plouzane, France. ⁶Norwegian Meteorological Institute, Research and Development, Oslo, 0313, Norway. ⁷University Centre of Svalbard, Longyearbyen, 9171, Norway. ✉e-mail: maltem@met.no

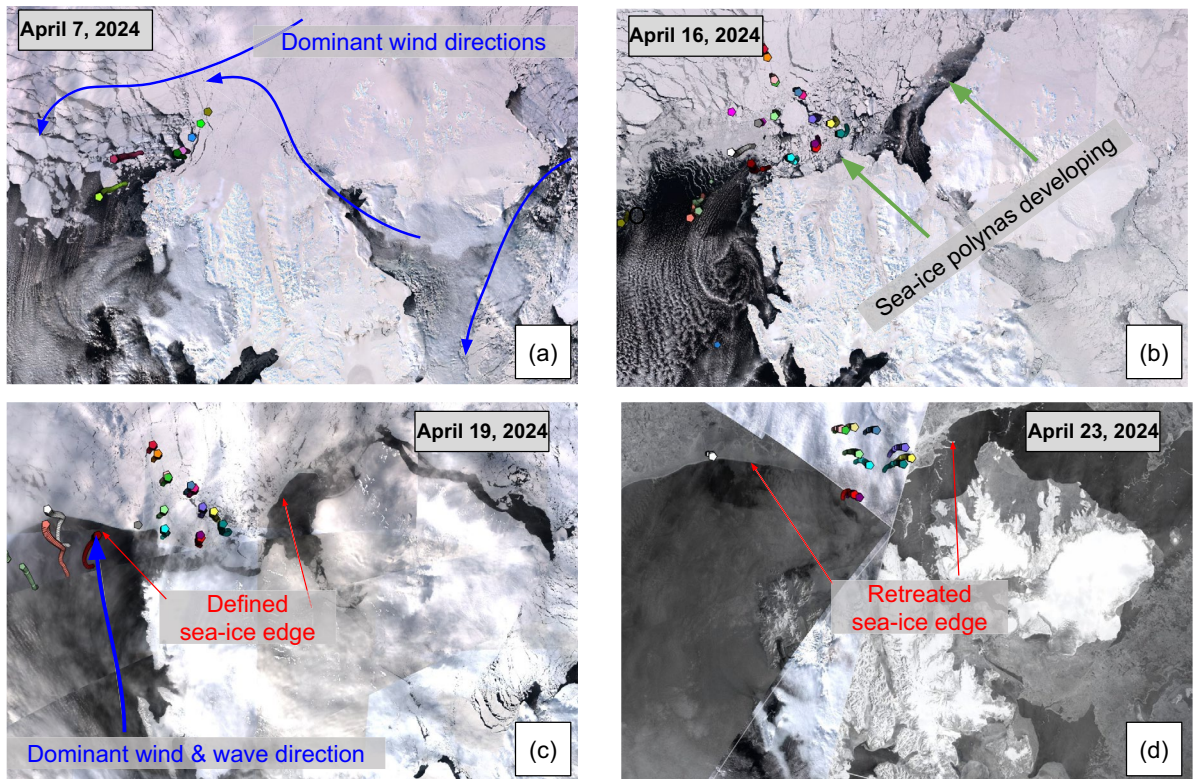


Fig. 1 Development of the sea ice conditions through wind and wave forcing from April 7 to 23, 2024 in the north of the Svalbard Archipelago. True color Sentinel-3 OLCI (a, b, and c) and Sentinel-1 SAR roughness (d) satellite images are shown. Colored points show buoy positions. Figure made by using OceanDataLab's Ocean Virtual Laboratory³⁶.

systems and the understanding of their key deficiencies. During the MOSAIC campaign, a distributed network of four atmospheric observation stations was deployed around RV Polarstern^{14,17}. Mean distances between the individual stations were on average between 11 and 34 km throughout the drift and gave new insights into spatio-temporal atmospheric variability over sea-ice and corresponding sub-grid scale variability of models¹⁸.

The Svalbard Marginal Ice Zone Campaign 2024 (SvalMIZ-24) aimed to establish a network of observational buoys north of the Svalbard Archipelago. The campaign focused on gathering data on temperature (air and surface), sea-ice drift, and wave energy spectra. Between April 4 and April 21, 2024, a total of 34 OpenMetBuoy¹⁹ (OMB) were deployed in the MIZ north of Svalbard using the Norwegian Coast Guard vessel KV Svalbard. The deployment region was selected to capture the evolution of ice conditions in response to varying meteorological and wave forcing. During the campaign, two distinct atmospheric regimes were observed (Fig. 1). First, a cold air outbreak (April 6–19, 2024) with strong northerly and easterly winds led to compact ice conditions and the formation of polynyas due to topographical effects on the wind patterns. Temperatures were low with values around -15°C . Second, a warm air intrusion event, with southerly winds (April 19–23, 2024) brought a temperature increase of about 15°C , strong winds and significant wave activity (>5 meters). These conditions led to ice breakup and a northward retreat of the ice edge.

Therefore, these observations capture two dynamic weather events and contain data that are particularly relevant for improving Arctic weather, wave and sea-ice models. This dataset²⁰ will support validation and inter-comparison studies of coupled model systems and, in the long-term, enhance the accuracy of predictions related to sea-ice dynamics, wave propagation, and atmospheric conditions in the MIZ and beyond.

Methods

The present dataset²⁰ is collected using the OpenMetBuoy-v2021¹⁹ (OMB-v2021), on which we add four temperature sensors (Fig. 2, see also²¹). The OMB is a free and open-source software and hardware instrument platform developed to collect oceanographic data that can be customized for specific applications. The core advantages of the OMB are that i) this design is fully open source, which allows for investigating all the processing performed, and gives a detailed understanding of the noise characteristics of the measurements. Moreover, ii) the OMB costs typically 10 times less than comparable commercial alternatives, which allows large scale deployments under a constrained budget. In addition, iii) the OMB can be customized with additional sensors, as is done here for the temperature measurements. Finally, iv) the OMB is particularly adapted to polar environments, since it is power efficient enough that it does not need to rely on solar panels that easily get covered by snow, it tolerates harsh temperatures, and its footprint reduces the risk of attracting polar bear attention, which otherwise usually results in destruction of scientific equipment.

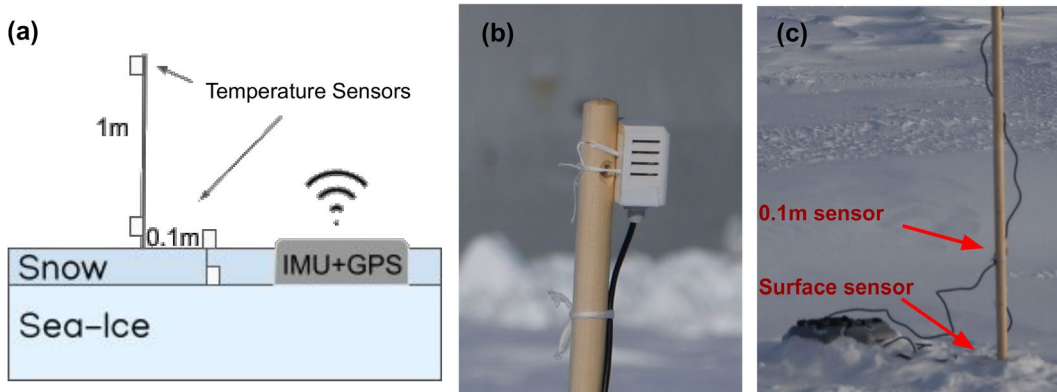


Fig. 2 (a) Illustration of the OMB-v2021 set up used during SvalMIZ-24 with four temperature sensors, (1) at the snow-ice interface, (2) at the snow surface, (3) at 0.1-meter height, and (4) at 1-meter height. (b) Radiation shield and temperature sensor mounted on a 1-meter pole. (c) The buoy set-up on an ice floe with surface and 0.1-meter temperature sensors.

In the first sub-section we describe the standard OMB version that primarily focuses on sea-ice or ocean drift and wave measurements. The second sub-section describes the addition of the temperature sensors and, finally, the third subsection is dedicated to additional measurements of sea-ice thickness, snow depth, and snow density, which were made at the time of deployment of each OMB.

Wave and sea ice drift. The standard OMB design builds on a long series of previous Inertial Motion Unit (IMU) based waves-in-ice buoys^{22–25}, and has been thoroughly discussed and validated in previous studies. For a detailed overview, see¹⁹ and references therein. Those seeking in-depth technical information can refer to the open-source implementation on GitHub <https://github.com/jerabaul29/OpenMetBuoy-v2021a>, as well as several studies using and further validating OMBs^{10,11,26,27}. Below, we present a concise summary of the OMB core design and functionality.

The OMB in its standard IP68 enclosure has a size of $10 \times 10 \times 12$ cm, and weighs between 0.5 and 1 kg depending on the number of batteries included. For the deployment described in this study, we used two D-cell lithium batteries, that give the buoy a lifetime of around 4.5 months without the need for an external solar panel. The core OMB design performs GPS position measurements every 15 minutes, and IMU-based wave measurements every 2 hours. Wave measurements are performed by sampling slightly above 20 minutes of motion data (so that the number of samples is a power of 2 and enables effective Fast Fourier Transforms (FFTs)). The motion sensor provides measurements of the buoy's acceleration and angular rates at 800Hz, and a combination of averaging and Kalman filtering is run on-the-fly on the main micro-controller unit to generate a 10Hz time series of the vertical wave elevation. This timeseries is finally processed using the Welch method, to generate the wave vertical acceleration spectrum. The data, encoded as binary messages for efficiency, are communicated back via iridium short burst data (SBD) satellite communications. A decoder is used on the receiver side to convert the Iridium messages back to float values, and generate both the vertical displacement spectrum and wave statistics.

Temperature. Four temperature sensors were added to the core OMB design. These are DS18B20 digital sensors (<https://www.analog.com/media/en/technical-documentation/data-sheets/ds18b20.pdf>), which operate via a 1-wire bus interface. Each sensor is assigned a unique 64-bit ID during production which can be queried over the communication bus, allowing to identify each sensor individually. Therefore, an arbitrary number of sensors can share the same bus and be identified individually, allowing to add as many sensors as necessary for the application considered. Moreover, the 64-bit ID allows to identify each sensor individually, and hence, to apply additional individual sensor calibration, as discussed lower down. The sensors were deployed so that they measured 1-meter air temperature, 0.1-meter temperature, snow surface temperature, and snow-ice interface temperature (see Fig. 2). In the following, we describe the individual calibration and accuracy of the DS18B20 measurements, as well as the setup of each of the four sensors.

Calibration and accuracy of DS18B20 sensors. The DS18B20 is a digital temperature sensor, which, compared to a thermistor such as a PT100 probe, does not require additional electronics to provide a reading and can be directly queried over a digital interface. Its datasheet absolute accuracy from the factory is only $\pm 0.5^\circ\text{C}$. Since errors of short-range weather prediction systems in the Arctic are around 1 to 5°C ^{28,29}, this is too inaccurate for our needs. However, the sensor can be asked to perform temperature measurements with a relative accuracy of up to 12 bits, resulting (given its datasheet measurement range) in a least significant bit resolution of 0.0625°C . We have performed in-depth testing of the DS18B20 to estimate its linearity and stationarity in the temperature range that is of interest for us (given the area in the MIZ and season considered, typically between -20°C and $+10^\circ\text{C}$). We have placed four DS18B20 sensors in a Stevenson screen at the Norwegian Meteorological Institute's test field in Oslo, alongside a reference calibrated PT100-based sensor. Since all sensors were placed in the same shield, the only source of discrepancy between temperature measurements from the different sensors comes from the inherent accuracies of the sensors. This test occurred during midwinter when cold temperatures

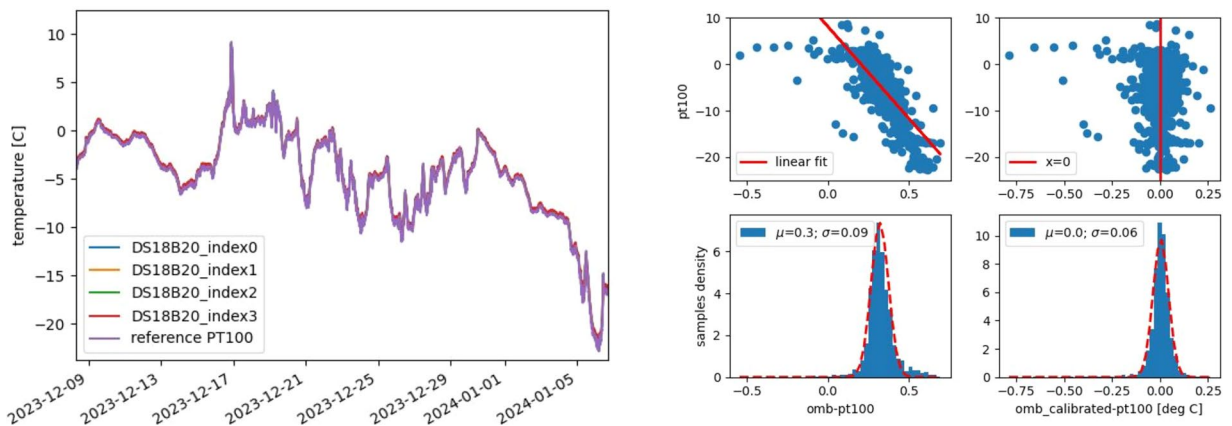


Fig. 3 Left: overview of the DS18B20 test period. The four DS18B20 sensors of one OMB (`DS18B20_index[0..3]`) were placed in a Stevenson shield alongside a reference calibrated PT100 probe. Around 4 weeks of data, spanning temperatures from around -20°C to around $+10^{\circ}\text{C}$, were collected. Right: analysis of the comparative temperature measurements obtained from one DS18B20 sensor, compared to the reference PT100. Similar results are obtained for all DS18B20 sensors. We show (top) the scatter plot for the mismatch between the DS18B20 and the PT100 as a function of temperature, both before (left) and after (right) linear calibration. The distribution for these mismatches is also provided (bottom). As visible there, the mismatch follows closely a Gaussian distribution. After linear calibration, the accuracy is comparable to the least significant bit resolution of the DS18B20.

prevail, providing a robust dataset for testing the accuracy of the DS18B20 sensor in temperature conditions similar to the MIZ in the spring. The DS18B20 sensors were logged by an OMB identical to what has been deployed in the field. In particular, a buck-boost converter is used to provide a stable 3.3 V supply to all the electronics of the OMB, including the DS18B20s. This means that there is no significant variability in the voltage supplied to the DS18B20 sensors, and that, in theory, the only factor influencing the temperature measurements is the actual temperature of the sensor.

The data gathered over a four-week test period are presented in a scatter plot in Fig. 3. In the left panel, we show the temperatures recorded by the PT100 and all four DS18B20 sensors over the test period. In the right panel, we show the detailed comparison between one DS18B20 sensor and the PT100. Similar results are obtained with the three other DS18B20s (though the offset and slope of the mismatch are individual to each sensor). Temperatures were between around -20°C and around $+10^{\circ}\text{C}$. Except for a couple of outlier readings, the mismatch between the PT100 reference sensor and the DS18B20 attached to the OMB is close to linear, and the distribution of the mismatch between the PT100 and the DS18B20 closely follows a Gaussian distribution. Therefore, a linear calibration can be defined, to map raw DS18B20 readings to calibrated DS18B20 readings, following:

$$T_c = T_b + s \cdot T_{\text{raw}}, \quad (1)$$

where T_c indicates the DS18B20 sensor considered following linear calibration, T_{raw} indicates the raw DS18B20 sensor reading, and T_b and s are obtained from the best linear fit matching the T_{raw} reading to the PT100 ground truth reading from the calibrated PT100 sensor.

As visible in Fig. 3, the typical standard deviation observed between the reference PT100 and the calibrated DS18B20 is 0.06°C , indicating that linear calibration typically is able to bring absolute accuracy close to the resolution of the least significant bit reported by the DS18B20. The calibration is individual to each DS18B20 sensor and, therefore, all buoys were subsequently deployed with their sensors placed in the same setup for at least 1 week, to generate the data necessary to calibrate each DS18B20 sensor individually on each buoy. Note that the accuracy reported here is only the accuracy of the sensor per se. The uncertainty introduced by the radiation shield is discussed in the next section.

Following this test, we conclude that a properly calibrated DS18B20 sensor can reach, with stable constant regulated voltage input, an absolute accuracy of the order of the numerical precision of its least significant bit, which is around a factor 10 more accurate than the sensor bought out-of-the-box and its factory calibration. This accuracy is deemed sufficient for our use, especially as other sources of uncertainty are significantly larger, as discussed below. In the following, all DS18B20 data reported are individually calibrated using this methodology, except if mentioned otherwise. For this, the calibration of each DS18B20 was matched to its unique 64-bit ID, and a calibration lookup was added to the iridium binary data decoding workflow.

In the following, we discuss the placement and properties of each of the four DS18B20 attached to each OMB.

1-meter air temperature. This DS18B20 sensor was mounted on a pole at 1-meter height within a small 3D-printed (white polylactic acid, PLA) radiation shield (Fig. 2b and <https://www.thingiverse.com/thing:4080321>). The radiation shield has been tested side-by-side with a PT100 reference temperature probe in a Gill-type radiation shield at the Norwegian Meteorological Institute's test field in Oslo from December 2023

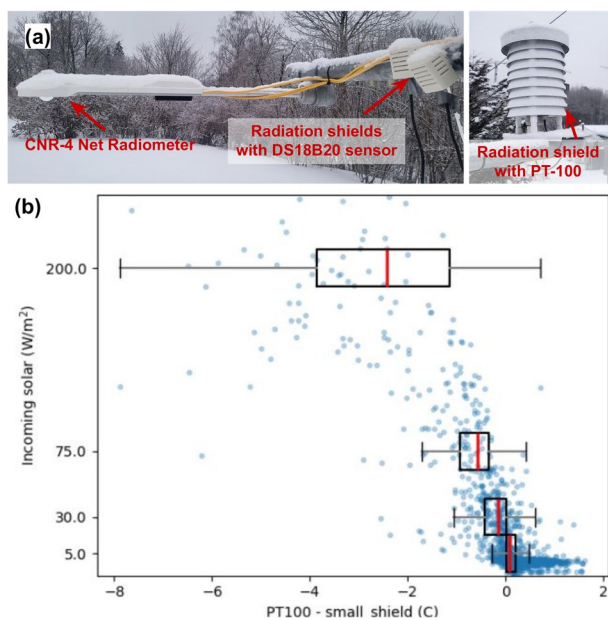


Fig. 4 The test station at the Norwegian Meteorological Institute’s in Oslo. (a) 3D-printed small radiation shields with DS18B20 sensors, CNR-4 net radiometer, and a reference Gill-type radiation shield with PT100 sensor are mounted at 2-meter height. (b) Temperature deviation between PT100 and DS18B20 ($T_{PT100} - T_{DS18B20}$) versus incoming solar radiation.

to February 2024. In addition, a Kipp & Zonen CNR4, a four-component net radiometer that measures incoming and outgoing shortwave and longwave radiation separately, was mounted at a distance of about 1-meter (Fig. 4a).

The validation of DS18B20 - small radiation shield versus the PT100 - Gill-type radiation shield shows a significant dependency on solar radiation (Fig. 4b). Observations in periods of solar radiation below 100 W/m^2 show a bias of less than 1°C , while for higher solar radiation values this bias increases to more than 2°C . Hence, we suggest that 1-meter temperature observations should be flagged when incoming solar radiation exceeds 100 W/m^2 . Thus, we include in the released data file the incoming solar radiation as simulated by the convective-scale weather prediction system AROME Arctic²⁸ collocated in space and time with the buoy temperature data records. The user of the data can decide which threshold to use, and we recommend flagging the air temperature measurements where radiation exceeds 100 W/m^2 . As a consequence of these limitations of the shield used, the temperature uncertainty is higher than the calibrated sensor’s intrinsic uncertainty discussed in the previous section.

0.1-meter air temperature. This sensor was mounted on the pole without a radiation shield at 0.1-meter height. The sensor was meant to be a reference sensor for the snow surface temperature sensor, to allow a detection of snow covering of the surface sensor in case of heavy snowfall.

snow surface temperature. This sensor was wrapped in copper tape to enhance its thermal conductivity and thus its ability to measure the snow-surface temperature. Previous tests with aluminum foil, white paint, and different variants of copper material showed that copper tape gives the best thermal coupling for snow surface temperature measurements. For one of the buoys (KVS-12), an individual validation on the sea ice was conducted with infrared sensors that had been mounted at the side of the ship approximately 5 meters above the surface of the ice floe on which KVS-12 had been deployed. A Campbell Science IR120 infrared sensor pointed at a 45-degree angle to the snow surface, for an atmospheric correction an Apogee SI-411 pointed at the same angle to the sky. The infrared measurements were conducted at a distance of about 200 meters from the buoy and for about 16 hours (Fig. 5). Generally, we find that, while the variability is captured, the surface measurements still need to be taken with care and are not directly comparable to IR measurements since the lowest negative temperatures are not observed and a positive bias occurs. Therefore, these data are only indicative.

snow-ice interface temperature. This sensor has been placed at the snow-ice interface, by digging a hole in the snow and sliding the sensor about 0.1 m along the snow-ice interface. Note, at some locations, the ice floe was already flooded with seawater, i.e. the lowest part of the snow layer has been soaked with seawater and thus the recorded temperature is at about the freezing temperature of -1.6°C .

Ice thickness, snow depth and density. Observations of sea-ice thickness, snow depth, and snow density were conducted at a site approximately 5 meters from each of the OMB stations (Fig. 6) Sea-ice thickness was measured after drilling a 5cm diameter hole with an ice auger. To assess snow density, vertical profiles of the snowpack were examined. Snow cores were extracted using a plastic tube with an 85 mm diameter. Multiple

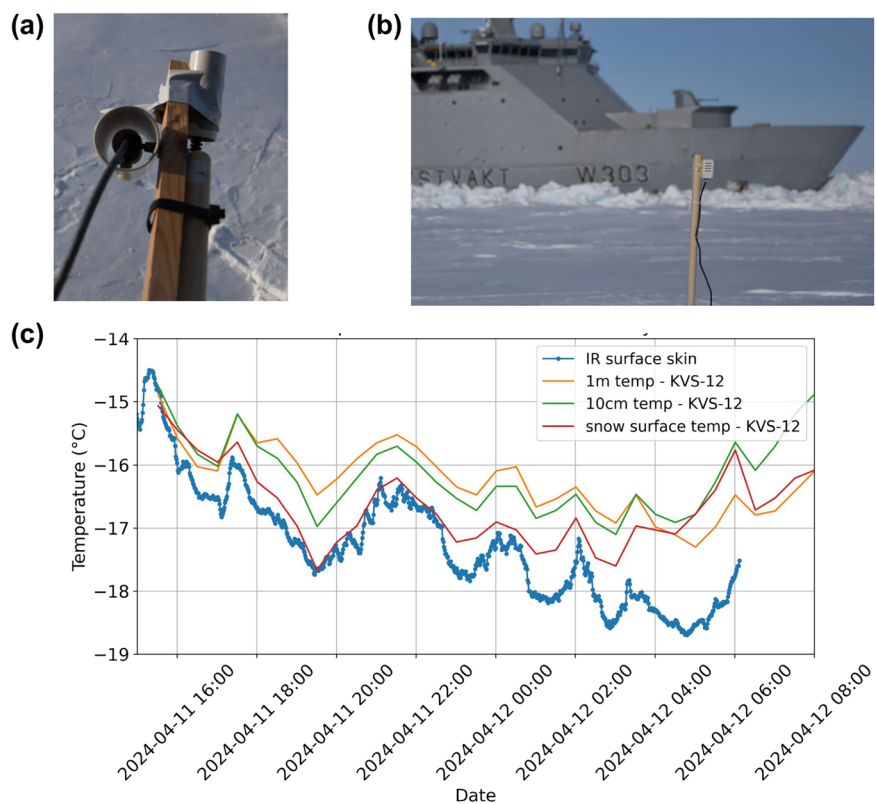


Fig. 5 The vessel KV Svalbard was moored at an ice floe where an OMB (KVS-12) had been deployed, about 200 meters toward the center of the floe (**b**). Data have been recorded from April 11, 2024, 16Z to April 12, 2024, 06Z with (**a**) infrared sensors mounted at the side of the ship and pointing toward the snow surface, as well as to the sky and from the OMB KVS-12. (**c**) The observed temperatures are from the four sensors on KVS-12 and from the infrared sensor observation.

cores were collected at each location to evaluate snow density. The number of cores varied depending on the snow depth and logistical constraints. Snow depth measurements were taken at two locations: one directly at the buoy and at the site about 5 meters away, where the snow cores were collected for density analysis. The snow density has been calculated onboard by weighing the snow samples.

Data Records

In total, 34 OMBs have been deployed on the sea ice north of Svalbard during a research cruise with the Norwegian Coast Guard ship KV Svalbard from April 4 to April 21, 2024. Due to a persistent cold air outbreak with predominantly northerly and easterly winds the sea ice was very compact in that area. The OMBs have been deployed along the ships' route to the furthest point in the northeast, in Hinlopenrennet, north of Hinlopen Strait. From that point, the ship returned, with a northward loop out of the Marginal Ice Zone on the 13th and 14th of April 2024. In that last part of the route, the final 16 buoys were deployed within 48 hours. Generally, the distance of the buoy location to the ice floe edge was about 50 to 100 m. Sites were chosen on rather flat areas and not too close to ridges.

During the main period of the campaign, two distinct weather regimes prevailed. The first period, from April 6 to April 19, was characterized by strong northerly to easterly winds and cold temperatures (around -20°C). The second period, from April 19 onward, saw a shift to southerly winds, accompanied by an increase in air temperatures of about 15°C and significant wave heights of more than 5 meters in the North Atlantic before propagating into the MIZ. The cold air outbreak with northerly winds before the campaign led to a compact sea-ice cover north of Svalbard and generally resulted in a positive sea-ice coverage anomaly around the Svalbard Archipelago compared to the climatological mean and standard deviation of error of the period from 1991 to 2020 (see also Fig. 8, Cruise Report²¹). From April 7 onward, easterly winds and the resulting southerly winds through Hinlopen Strait gradually caused the sea ice to break up, forming polynyas north of Spitsbergen and Nordaustland (Fig. 1b). The shift to warmer southerly winds and larger waves eventually led to a well-defined sea-ice edge and a northward retreat of the sea-ice (Fig. 1c). By April 23, the north side of Svalbard was detached from the Marginal Ice Zone, leaving only a zone of fast ice (Fig. 1d).

The trajectories of all buoys, showed on top of a snapshot of the sea ice concentration obtained from the AMSR2 product at the date April 4, 2024 00Z, are presented in Fig. 7. The time-dependent temperature development as the mean temperature over all buoys is shown in Fig. 8a and the transition from temperatures of around -15°C to temperatures of around 0°C is obvious. In the period between April 8 to May 1, 2024, between 6 to 20 buoys were operating in parallel and providing 1-meter air temperature, wave, and sea ice drift measurements,

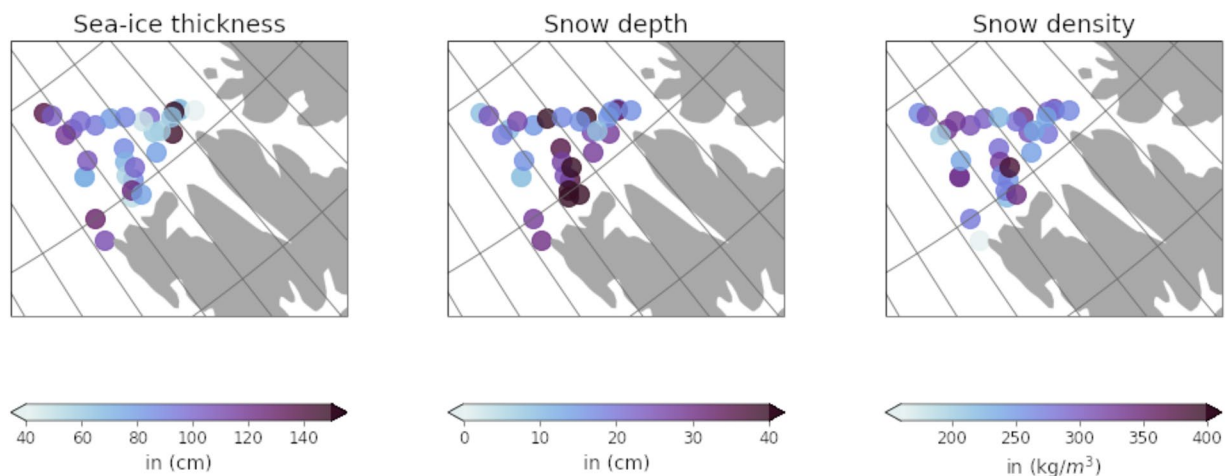


Fig. 6 Sea-ice thickness, snow depth (measurement co-located with snow density), and the snow density distribution observed during the deployment of the buoys from April 6 to April 14, 2024.

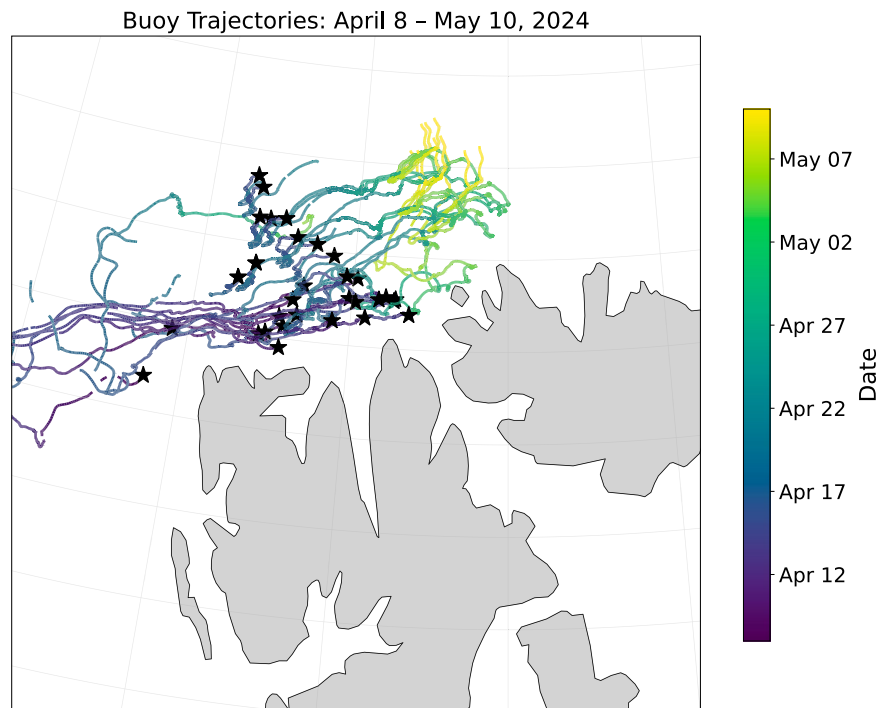


Fig. 7 Overview of the trajectories of the 34 OMBs deployed during the SvalMIZ-24 experiment. Trajectories are shown in the time period April 9 to May 10, 2024, and the * indicates the buoy deployment location.

that passed all quality control stages (see next section). In a peak phase of about 13 days ten or more buoys were operating in parallel and the mean distances of the buoys were between 40 and 100 km (Fig. 8a,b). In Fig. 9, wave energy spectra for three buoys at increasing distance into the MIZ at the beginning of the deployment are presented.

The data are made available as netCDF-CF files (for the OMB-generated data) and CSV files (for the *in-situ* snow properties measurements done during the deployment of each buoy) on Zenodo at the following URL: <https://zenodo.org/records/15312810> see also²⁰. Moreover, the raw binary Iridium SBD message data, processing scripts used to analyze these, and packaging scripts used to generate the netCDF files, are available on GitHub at the following URL: https://github.com/jerabaul29/2025_Svalbard_MIZ_KVS_SvalMIZ24. The data processing pipelines used to convert the binary Iridium SBD messages into netCDF-CF files are provided by the open source Trajectory Analysis (TrajAn) package and its OMB reader integration, which are available at: <https://github.com/OpenDrift/trajan>.

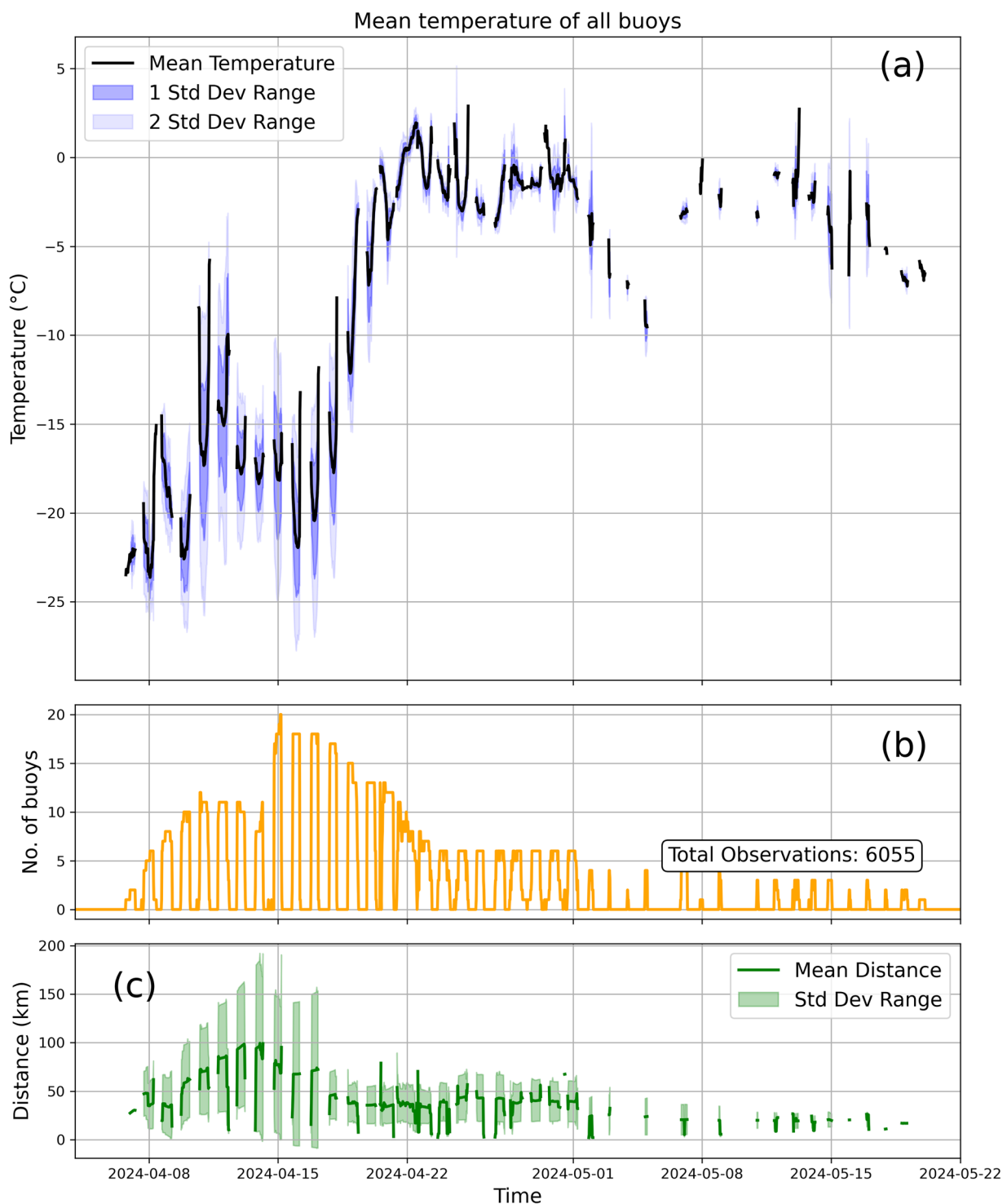


Fig. 8 Overview of the quality-controlled (threshold 100 W/m^2) temperature observations. In (a), the mean temperature of all buoys and the first and second standard deviations are shown. Note that the gaps in the time series are due to quality control. In (b), the number of buoys that provided those observations, and (c) the mean distance and standard deviation between those buoys are illustrated.

Technical Validation

The standard OMB-v2021 (excluding the temperature sensors, which are described in details above) that has been used in the present study has been validated and used in many studies before, see in particular the technical development paper¹⁹, the previous data release papers^{10,11}, and a number of scientific publications^{26,27}. The OMBs used here have exactly identical design from both a hardware and software perspective and, therefore, no more technical validation is necessary, and we refer the reader curious of technical details to the corresponding publications. Position and wave information are provided in the same format as in the earlier data release

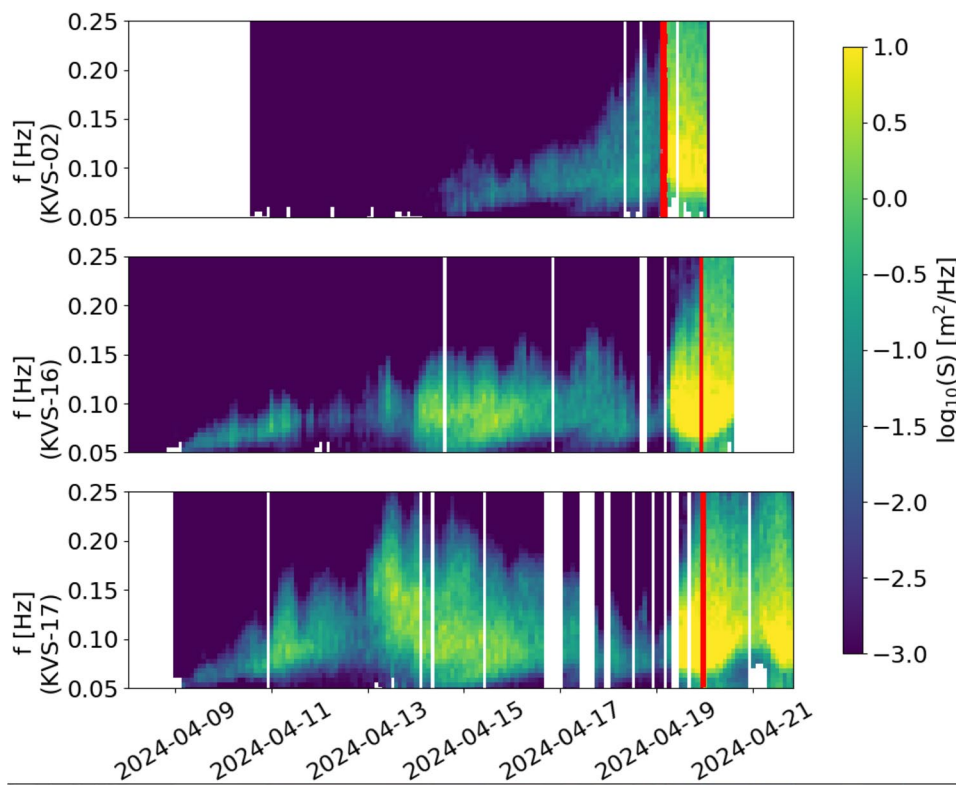


Fig. 9 Illustration of the wave spectra recorded by three buoys at different depths in the MIZ is shown. The red line indicates the sudden increase in high-frequency wave energy content, and the transition of the buoys to open water or the very open MIZ.

flag	description
temp_con_quality_flag	Conservative quality flag for temperature observations
temp_1m_quality_flag	Quality flag for temperature observations 1 m above the surface
rsds	AROME Arctic ²⁸ - Downward surface short-wave radiation (W/m^2)
sicon	AMSR2 - sea ice concentration ³⁰

Table 1. Quality flags and atmospheric and sea-ice properties to be used to flag the temperature observations.

papers^{10,11}. The GNSS position measurement is provided directly by a well-established chip, and no more technical validation is needed. The wave vertical spectrum and statistics are computed using an established methodology, which has been described in the literature on many occasions, as previously pointed out. More specifically, the OMB has been validated in the laboratory against test bench instrumentation, in the field against altimeter satellite data, and in the field against commercial buoys¹⁹. This has confirmed the ability of the OMB to measure waves down to typically 0.5 cm amplitude at a 16 s period, as mentioned above (see¹⁹).

The use of the DS18B20 temperature sensors is new to the OMB-v2021 setup (Fig. 2). The evaluation of the DS18B20 sensor neglecting radiative effects, i.e. the sensor is located in the same radiation shield as the PT100 reference sensor, shows that the accuracy is, with $\pm 0.1^\circ\text{C}$, sufficiently high after calibration (see previous section). However, when using the sensor in the technical setup in the field the following details need to be further considered for quality control: (1) the radiation shielding for the 1-meter air temperature, (2) the potential breaking of the ice floe or submerging by seawater, and (3) the thermal coupling of the surface temperature sensor to the snow surface and its exposure to solar radiation. For the various flags and other helpful OMB properties, please see also Tables 1 and 2.

Solar radiation impact on 1-meter air temperature. In the previous section, the impact of the solar radiation shield on the air temperature measurements at the test station has been described (Fig. 4). The calibrated observations have a positive bias below 1°C when measurements during solar radiation above $100 W/m^2$ are ignored. Since solar radiation is not measured in our OMB setup we need to estimate this from a model system. Solar radiation at buoy locations has been extracted from the operational convective-scale weather forecasting system AROME Arctic and is provided in the data release on the same time axis as the temperature observations. Thus, the user of the data can define and do sensitivity studies with individually defined thresholds of solar incoming radiation.

size (default box)	10 × 10 × 12 cm
weight (battery and box dependent)	0.5-1.0 kg
microcontroller	Ambiq Apollo 3
communications	Iridium SBD
GNSS chip	ZOE-M8Q
motion sensor chip	ISM330DHGX
temperature sensors	DS18B20
battery	2 LSH20
autonomy	4+ months
GNSS sample rate	once every 30 minutes
wave 1D spectrum sample rate	once every 2 hours
temperature sample rate	every 30 minutes
motion sensor raw data rate	800 Hz
Kalman filter refresh rate	100 Hz
wave acceleration sample rate	10 Hz
wave spectrum data sample duration	20.48 minutes
temperature sensor type	DS18B20
typical intrinsic calibrated temperature accuracy	± 0.0625 degrees C
number of temperature sensors	4: 1-meter air, 0.1-meter air, snow surface, snow-ice interface
online open source project repository	https://github.com/jerabaul29/OpenMetBuoy-v2021a

Table 2. Key properties of the OMB-v2021 plus temperature sensors that was used for SvalMIZ-24.

Contact with seawater. Most of the buoys will be in contact with sea water after a certain amount of time when seawater floods the floe due to break-up, melting, loading by snow, or ridging. In particular for the temperature observations and their representation of the different conditions (air, surface, snow-ice interface) this is important. Utilizing an objective method to do such quality control was not possible due to the manifold of scenarios that are possible and can lead to failures in the temperature reading or their representativeness. Hence, we inspected each time series individually, to identify the following kinds of events: i) when sensors stop working (hardware failure), ii) when a large jump in data is observed in contrast to the weather forecast data, iii) when values being measured are constant and close to the seawater temperature of -1.6°C , and iv) when the buoy is in an area of very low sea ice concentration values indicated by a high-resolution AMSR2 based product³⁰. In addition, the wave spectra have been used to identify buoys that are in open water, using the fact that the energy content in the high-frequency part of the spectra is significantly damped when buoys are located in the sea ice compared to the open water conditions.

From this, two sets of quality flags are derived:

- temp_con_quality_flag: This is the conservative flag. It is raised if there is a suspicion that the sea ice has been flooded, e.g. when the snow-ice interface sensor remains quite constant around -1.6°C , or changes in the high-frequency wave energies are noted. If one of the temperature sensors significantly malfunctions or shows a large jump, this flag is raised, even when other sensors still seem reliable.
- temp_1m_quality_flag: This is an alternative set of slightly less restrictive quality flags, designed to conserve 1-meter temperature values that still seem reasonable, even though other sensors might have already become unreliable due to, e.g., flooding.

Thermal coupling and radiation of surface measurements. As shown in the previous section and Fig. 5, the accuracy of the surface temperature values is limited due to radiative effects and issues with thermal coupling to the surface. They are impacted directly by solar radiation (not shown) and are not able to show the lowest temperatures compared to infrared sensor-based observations.

Usage Notes

GPS position data can be used without further considerations, as the GPS module itself performs all the data quality assurance necessary, and the position accuracy is more than enough to resolve trajectories given the 30 minute sample rate.

Similarly to other acceleration-based wave measurements, and in good agreement with the motion sensor datasheet, the OMB exhibits an acceleration noise spectral density that is constant (i.e., independent of frequency). As a consequence, the noise level for the wave elevation spectral density, which is obtained by integrating elevation twice in time, shows increased noise level in the low frequency range. This is a well-known effect^{19,31,32}. In order to mitigate this effect, we transmit wave vertical acceleration spectra over iridium, so that the raw acceleration spectra are available to the end user. Elevation spectra are computed from the acceleration spectra using a Python script that is included in the OMB GitHub repository. This enables the user to observe the unfiltered noise level present in the wave spectra, before any further processing is applied. Our data processing code also generates a low frequency cutoff estimate to take into account this low frequency noise

link	URL
GitHub: OMB main page	https://github.com/jerabaul29/OpenMetBuoy-v2021a
commercial OMB	https://www.labmaker.org/products/openmetbuoy
GitHub: data release	https://github.com/jerabaul29/2025_Svalbard_MIZ_KVS_SvalMIZ24
GitHub: MIZ data overview	https://github.com/jerabaul29/meta_overview_sea_ice_available_data
GitHub: TrajectoryAnalysis	https://github.com/OpenDrift/trajan
data release archive	https://zenodo.org/records/15312810

Table 3. URLs for webpages, data and code release.

amplification. This cutoff is obtained as the first local minimum, if such a minimum exists, observed between the lowest-frequency bin and the peak of the wave elevation spectrum, as previously described in³¹. This allows us to separate between actual signal and noise. We underline that the unfiltered acceleration power spectral density data are always available to the user so that a visual inspection of each individual spectrum before any filtering can be performed if necessary. Moreover, the code used for generating this low-frequency cutoff is part of the open source code we provide, so it can be inspected by the user.

With respect to the 1-meter temperature measurements, we recommend using one of the temperature flags provided with the data (Table 1), as well as a threshold for the incoming solar radiation. For the latter, we recommend to use the value of 100 W/m² or smaller. The snow surface measurement must be seen as experimental and inaccuracies larger than 1 °C, in particular, biases due to insufficient thermal coupling and solar radiation effects, can occur. The data might be interesting for some users, assessing spatiotemporal variability in comparison to remote sensing or model products, but conclusions from that must be taken with care. The 0.1-meter temperature has no radiation shielding and can be used for additional flagging purposes or other assessments. However, it is exposed to sunlight and thus might only be used as an indicator for ice floe flooding or snowfall. The snow-ice interface temperature is not exposed to sunlight and temperature coupling and radiation effects are not an issue with this sensor. Note, that the snow depth at the site where this sensor is located is related to the snow-depth measurement no.2.

Code availability

The OMB-v2021 used to collect all the data released here is fully open source. The hardware, firmware, and data post-processing details are available in the public GitHub repository of the project: <https://github.com/jerabaul29/OpenMetBuoy-v2021a>. The OMB firmware can be compiled with the Arduino IDE v1.8.19 available at <https://www.arduino.cc/en/software> (see instructions on the OMB GitHub repository for library installations). The buoy firmware is written in C++, while post-processing tools and data decoders are written in Python3.

The code used to format and prepare the data released in this paper is available on the public GitHub repository associated with this article: https://github.com/jerabaul29/2025_Svalbard_MIZ_KVS_SvalMIZ24. This code is written in Python3, and does heavy use of the Trajectory Analysis (TrajAn) software package <https://github.com/OpenDrift/trajan>. For details see also Table 3.

Similarly to previous OMB data releases, we will offer reasonable support regarding the data and its use through the Issues tracker of the data repository associated to this article at https://github.com/jerabaul29/2025_Svalbard_MIZ_KVS_SvalMIZ24. Moreover, we invite readers in need of specific help to contact us there. We invite scientists who own similar data and are willing to release these as open data and open source materials to contact us so that they can get involved in the next data release we will perform, and we hope to be able to support and encourage further community-wide data releases in the future.

While there are already a significant number of datasets available about sea ice drift and waves in ice (for example,^{10,33–35}), these are scattered across the internet, and often hard to find. Therefore, we maintain an index of similar data at https://github.com/jerabaul29/meta_overview_sea_ice_available_data. We invite readers aware of additional similar data to submit an issue or pull request on the corresponding GitHub repository, adding additional pointers to similar datasets.

Received: 12 May 2025; Accepted: 26 August 2025;

Published online: 30 September 2025

References

- Isaksen, K. *et al.* Recent warming on Spitsbergen— influence of atmospheric circulation and sea ice cover. *J. Geophys. Res. Atmos.* **121**, 11,913–11,931 (2016).
- Kwok, R. Arctic sea ice thickness, volume, and multiyear ice coverage: losses and coupled variability (1958–2018). *Environ. Res. Lett.* **13** (2018).
- Rolph, R. J., Feltham, D. L. & Schröder, D. Changes of the arctic marginal ice zone during the satellite era. *The Cryosphere* **14**, 1971–1984, <https://doi.org/10.5194/tc-14-1971-2020> (2020).
- Song, L., Zhao, X., Wu, Y., Gong, J. & Li, B. Assessing Arctic Marginal Ice Zone dynamics from 1979 to 2023: insights into long-term variability and morphological changes. *Environmental Research Letters* **20**, 034032 (2025).
- Thomson, J. & Rogers, W. E. Swell and sea in the emerging Arctic Ocean. *Geophys. Res. Lett.* **41**, 3136–3140 (2014).
- Müller, M., Knol-Kauffman, M., Jeuring, J. & Palerme, C. Arctic shipping trends during hazardous weather and sea-ice conditions and the Polar Code's effectiveness. *npj Ocean Sustainability* **2**, 12 (2023).
- Itkin, P. *et al.* Thin ice and storms: Sea ice deformation from buoy arrays deployed during N-ICE2015. *J. Geophys. Res.* **122**, 4661–4674, <https://doi.org/10.1002/2016JC012403> (2017).

8. Kohout, A. L. *et al.* Observations of exponential wave attenuation in antarctic sea ice during the pipers campaign. *Annals of Glaciology* **61**, 196–209, <https://doi.org/10.1017/aog.2020.36> (2020).
9. Kaleschke, L. & Müller, G. Sea ice drift from autonomous measurements from 15 buoys, deployed during the IRO2/SMOSIce field campaign in the barents sea march 2014 (2022).
10. Rabault, J. *et al.* A dataset of direct observations of sea ice drift and waves in ice. *Scientific Data* **10**, 251, <https://doi.org/10.1038/s41597-023-02160-9> Publisher: Nature Publishing Group (2023).
11. Rabault, J. *et al.* A position and wave spectra dataset of Marginal Ice Zone dynamics collected around Svalbard in 2022 and 2023. *Scientific Data* **11**, 1417 (2024).
12. Granskog, M. A. *et al.* Arctic research on thin ice: Consequences of Arctic sea ice loss. *Eos* **97**, 22, <https://doi.org/10.1029/2016EO044097> (2016).
13. Renfrew, I. A. *et al.* An evaluation of surface meteorology and fluxes over the iceland and greenland seas in ERA5 reanalysis: The impact of sea ice distribution. *Quarterly Journal of the Royal Meteorological Society* **147**, 691–712, <https://doi.org/10.1002/qj.3941> (2021).
14. Shupe, M. D. *et al.* Overview of the MOSAiC expedition: Atmosphere. *Elementa: Science of the Anthropocene* **10**, 00060 (2022).
15. Mages, Z., Kollias, P., Zhu, Z. & Luke, E. P. Surface-based observations of cold-air outbreak clouds during the comble field campaign. *Atmospheric Chemistry and Physics* **23**, 3561–3574, <https://doi.org/10.5194/acp-23-3561-2023> (2023).
16. Seidl, A. W. *et al.* The ISLAS2020 field campaign: Studying the near-surface exchange process of stable water isotopes during the arctic wintertime. *Earth System Science Data Discussions* **2024**, 1–35, <https://doi.org/10.5194/essd-2024-293> (2024).
17. Rabe, B. *et al.* The mosaic distributed network: Observing the coupled arctic system with multidisciplinary, coordinated platforms. *Elementa: Science of the Anthropocene* **12**, 00103, <https://doi.org/10.1525/elementa.2023.00103> (2024).
18. Herrmannsdörfer, L., Müller, M., Shupe, M. D. & Rostosky, P. Surface temperature comparison of the Arctic winter MOSAiC observations, ERA5 reanalysis, and MODIS satellite retrieval. *Elementa* **11**, 00085, <https://doi.org/10.1525/elementa.2022.00085> (2023).
19. Rabault, J. *et al.* Openmetbuoy-v2021: An easy-to-build, affordable, customizable, open-source instrument for oceanographic measurements of drift and waves in sea ice and the open ocean. *Geosciences* **12**, 110, <https://doi.org/10.3390/geosciences12030110> (2022).
20. Müller, M., Rabault, J., Palerme, C. & de de Geeter, C. Dataset: Svalbard Marginal Ice Zone Campaign 2024 - a distributed network of temperature, waves in ice, and sea ice drift observations. *Zenodo*, <https://zenodo.org/records/15312810> (2025).
21. Müller, M., Rabault, J. & Palerme, C. Svalbard Marginal Ice Zone 2024 campaign - cruise report. *arXiv* <https://doi.org/10.48550/arXiv.2407.18936> (2024).
22. Rabault, J. *et al.* Measurements of waves in landfast ice using inertial motion units. *IEEE Transactions on Geoscience and Remote Sensing* **54**, 6399–6408 (2016).
23. Sutherland, G. & Rabault, J. Observations of wave dispersion and attenuation in landfast ice. *Journal of Geophysical Research: Oceans* **121**, 1984–1997 (2016).
24. Rabault, J., Sutherland, G., Gunderson, O. & Jensen, A. Measurements of wave damping by a grease ice slick in svalbard using off-the-shelf sensors and open-source electronics. *Journal of Glaciology* **63**, 372–381 (2017).
25. Rabault, J. *et al.* An open source, versatile, affordable waves in ice instrument for scientific measurements in the polar regions. *Cold Regions Science and Technology* **170**, 102955 (2020).
26. Takehiko, N. *et al.* A comparison of an operational wave-ice model product and drifting wave buoy observation in the central arctic ocean: investigating the effect of sea-ice forcing in thin ice cover. *Polar Research* **42**, <https://doi.org/10.33265/polar.v42.8874> (2023).
27. Nose, T. *et al.* Observation of wave propagation over 1,000 km into Antarctica winter pack ice. *Coastal Engineering Journal* **66**, 115–131 (2024).
28. Müller, M. *et al.* Characteristics of a convective-scale weather forecasting system for the European Arctic. *Mon. Wea. Rev.* **145**, 4771–4787, <https://doi.org/10.1175/MWR-D-17-0194.1> (2017).
29. Müller, M., Batrak, Y., Dinessen, F., Grote, R. & Wang, K. Challenges in the description of sea ice for a kilometer-scale weather forecasting system. *Weather and Forecasting* **38**, 1157 – 1171, <https://doi.org/10.1175/WAF-D-22-0134.1> (2023).
30. Rusin, J., Lavergne, T., Doulgeris, A. P. & Scott, K. A. Resolution enhanced sea ice concentration: a new algorithm applied to AMSR2 microwave radiometry data. *Annals of Glaciology* **65**, e15, <https://doi.org/10.1017/aog.2024.6> (2025).
31. Waseda, T. *et al.* Arctic wave observation by drifting type wave buoys in 2016 (OnePetro, 2017).
32. Nose, T., Webb, A., Waseda, T., Inoue, J. & Sato, K. Predictability of storm wave heights in the ice-free Beaufort Sea. *Ocean Dynamics* **68**, 1383–1402, <https://doi.org/10.1007/s10236-018-1194-0> ADS Bibcode: 2018OcDyn..68.1383N (2018).
33. Kohout, A. & Williams, M. Waves in-ice observations made during the SIPEX II voyage of the aurora australis, 2012. Australian Antarctic Data Centre, Accessed: 2022-09-12 (2015).
34. Thomson, J. Long-term measurements of ocean waves and sea ice draft in the central Beaufort Sea. University of Washington Works Archive, Accessed: 2022-09-12 (2020).
35. Thomson, J. *et al.* Data to accompany the article “Wave-driven flow along a compact Marginal Ice Zone”. University of Washington Works Archive, Accessed: 2022-09-12 (2020).
36. Collard, F. *et al.* Ocean virtual laboratory: A new way to explore multi-sensor synergy demonstrated over the agulhas region. In *Proceedings of Sentinel-3 for Science Workshop (2–5 June 2015, Venice, Italy)* (ESA, 2015).

Acknowledgements

We acknowledge the support of the Research Council of Norway for the FOCUS project (RCN-301450) and FOCUS-FieldStudy (RCN-349619), the WMO-PCAPS project, and the Norwegian Meteorological Institute. We thank the Norwegian Coast Guard for offering crucial support for research in the Arctic and the crew of KV Svalbard for their invaluable help during fieldwork and instrument deployment. This article is a contribution to the Polar Coupled Analysis and Prediction for Services (PCAPS), a flagship project of the World Weather Research Programme (WWRP) of the World Meteorological Organization (WMO). We acknowledge the WMO WWRP for its role in coordinating this international research activity.

Author contributions

M.M. and J.R. were the main initiators of the manuscript and designed the data collection. M.M. was leading the project and the campaign. J.R. put the data in the common format, prepared the technical aspects. C.G. performed the quality control and flagging of the data. B.C.B., O.W., and S.E. contributed to the validation and testing of the temperature sensors. F.C., S.H., and G.H. contributed to the data gathering and dissemination. N.H., M.J., J.K., F.N. contributed to the logistics before and during the campaign. M.M. and J.R. wrote the manuscript, with help from C.G., and feedback from all co-authors. All authors reviewed the manuscript and participated in iterating the manuscript.

Competing interests

The authors declare no competing interests.

Additional information

Correspondence and requests for materials should be addressed to M.M.

Reprints and permissions information is available at www.nature.com/reprints.

Publisher's note Springer Nature remains neutral with regard to jurisdictional claims in published maps and institutional affiliations.



Open Access This article is licensed under a Creative Commons Attribution-NonCommercial-NoDerivatives 4.0 International License, which permits any non-commercial use, sharing, distribution and reproduction in any medium or format, as long as you give appropriate credit to the original author(s) and the source, provide a link to the Creative Commons licence, and indicate if you modified the licensed material. You do not have permission under this licence to share adapted material derived from this article or parts of it. The images or other third party material in this article are included in the article's Creative Commons licence, unless indicated otherwise in a credit line to the material. If material is not included in the article's Creative Commons licence and your intended use is not permitted by statutory regulation or exceeds the permitted use, you will need to obtain permission directly from the copyright holder. To view a copy of this licence, visit <http://creativecommons.org/licenses/by-nc-nd/4.0/>.

© The Author(s) 2025